Progress In Electromagnetics Research C, Vol. 115, 65–80, 2021

T-Shaped Tri-Band Antenna Based on Characteristic Mode Analysis for Satellite Applications

Fateh L. Lohar[1, *], Indra B. Sharma[2], Virender Katewa[3], and Mahendra M. Sharma[2]

Abstract—This article presents a T-Shaped Tri-Band (TSTB) antenna based on the Characteristic Mode Analysis (CMA) for satellite applications. Tri-band characteristics are achieved by exciting two orthogonal radiating modes for the L5-band and L1-bands, and one higher order radiating mode for the S-band. Initially, cavity model theory is applied to a rectangular antenna to calculate orthogonal modes (TM^z_{010} & TM^z_{001}) at L5-band and S-bands, and these modes are validated using the CMA method. With the help of surface current study and modification of a rectangular antenna, the one higher order radiating mode and orthogonal modes are excited by using the CMA method. All desirable radiating modes are excited by a single coaxial feed line in full-wave simulation, which is based on FIT (Finite Integration Technique). The proposed antenna's measured operating frequencies are 1575 MHz (L1-band) for GPS (Global Positioning System) system, 1174 MHz (L5-band), and 2495 MHz (S-band) for IRNSS (Indian Regional Navigation Satellite System) applications, and corresponding impedance bandwidths at $S_{11} \leq -10$ dB are 24 MHz (1563–1587 MHz), 24 MHz (1164–1188 MHz), and 51 MHz (2484–2535 MHz), respectively. The proposed antenna layout is printed on low-cost FR4 material and exhibits good agreement between simulated and measured results using CST and HFSS EM-tool. The proposed antenna is single feed, low profile, and economical with stable broadside radiation patterns along with good gain.

1. INTRODUCTION

Nowadays, with the rapid development of cutting-edge technology in modern wireless communication systems, the demand for multi-band antennas with excellent performance, light weight, and ease of integration with RF front-ends has grown. Satellite-based navigation systems are one of the most successful wireless systems. GPS is a well-known satellite based navigation system to provide geo-location to GPS receivers around the earth, which is controlled by the U.S government. Other countries also have deployed their navigation satellite systems to space, such as IRNSS (India), GLONASS (Russia), Galileo (EU), BeDou (China), and QZSS (Japan) [1]. The IRNSS is the new Indian space based positioning and navigational system, which is being developed by the Indian Space Research Organization (ISRO). The IRNSS provides better accuracy in position, time, and velocity information in real time applications because this system uses seven satellite constellations and has the operating frequency of L5-band (1176.45 MHz) and S-band (2492.08 MHz). It has an accuracy of up to 10 meters in the Indian region and 20 meters in the Indian Ocean region, and coverage up to 1500 kilometers from the primary Indian region [2, 3].

A tri-band operation is obtained by combining the IRNSS bands (L5-band and S-band) with the GPS band, which is in high demand in the current Indian situation. Multi-band reception antennas are

Received 22 July 2021, Accepted 20 August 2021, Scheduled 30 August 2021

* Corresponding author: Fateh Lal Lohar (fatehudml@gmail.com).

[1] Department of Electronics Communication Engineering, Govt. Engineering College Jhalawar, India. [2] Department of Electronics and Communication Engineering, Malaviya National Institute of Technology, Jaipur, India. [3] Vikram Sarabhai Space Centre, ISRO, Kerala, India.

required to receive multiple-band signals from multi-mode satellites such as for IRNSS and GPS tri-band (L5-band, S-band, and L1-band) receiver antennas [4–6]. Many organisations and researchers are working on dual- and tri-band IRNSS and GPS antennas for civilian, defence, and military applications. Microstrip patch antennas are reliable due to its favorable characteristics such as compactness, light weight, low cost, small size, and ease of circuit integration [7, 8]. Compact and light-weight multi-band antennas are highly demanded for navigation satellite applications, which are operated under multiple frequencies having similar features at all the frequency bands, such as hemispherical radiation patterns with stable phase centre [9, 10].

Many methods for designing multi-band antennas have been reported in the previous literature, such as the resonator loaded slot multi-band antenna reported in [11], triple-band antenna design using annular ring reported in [12], multi-band antenna design based on Genetic Algorithm reported in [13], dual-band circularly polarized DRA (Dielectric resonator antenna) for sub-6 GHz reported in [14], multi-band slot antenna design reported in [15–17], hexagonal gasket fractal multi-band antenna reported in [18, 19], multi-band antenna design using Defected Ground Structure (DGS) reported in [20–22], and low profile multi-band PIFA antenna design reported in [23]. These antennas have many advantages, but there are some performances still to be improved, such as poor radiation properties (backside radiation, non-stable radiation for each band, large minor lobes), cost, and complexity for integration in circuits.

Tri-band characteristics are accomplished in this work by separating two orthogonal modes for the L5-band and L1-band. One S-band is achieved by exciting higher order in broadside radiation by using the CMA method, and it performs well in satellite receiver applications due to its single-feed, low-profile, and economical design with stable radiation patterns and good gain.

2. TSTB ANTENNA DESIGN METHODOLOGY AND OPERATIONAL MECHANISM

2.1. Modal Analysis of Antenna Using Cavity Model Method (CMM)

2.1.1. Cavity Model Method Discussion

In the past decade, a lot of methods have been developed to determine the resonant modes or far-filed radiation characteristics of microstrip antenna. These methods are categorized into two types. One is analytical solution, and the second is full-wave analysis method. The cavity model approach is an analytical approach that offers good intuitive explanations of microstrip antennas using fundamental assumptions; however, it is difficult to apply to irregularly shaped microstrip antennas. The full-wave analysis method can be used for arbitrarily shaped microstrip antenna to provide accurate results by solving Maxwell's equations with particular boundary conditions [24].

In this method, patch antenna looks like dielectric-loaded cavity and has dominant and higher order

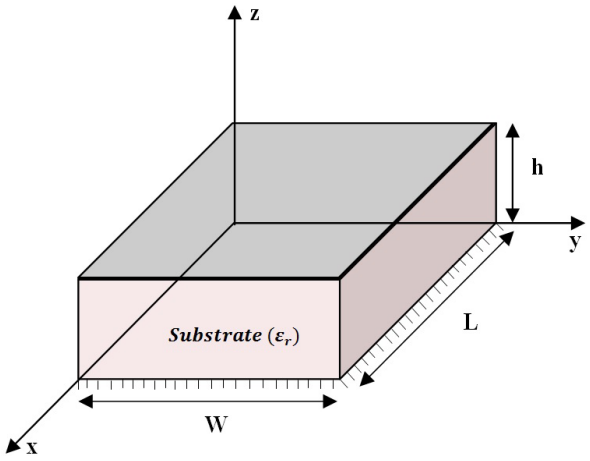

Figure 1. Cavity model of rectangular antenna.

resonance modes. The normalized fields within the dielectric substrate can be calculated more precisely by using the electric boundary (above and below the cavity) and magnetic boundary (circumference of the cavity) shown in Figure 1. The resonance frequency of TM^z for cavity is given by as [25]:

$$(f_r)_{mnp} = \frac{1}{2\pi\sqrt{\mu\epsilon}}\sqrt{\left(\frac{m\pi}{h}\right)^2 + \left(\frac{n\pi}{L}\right)^2 + \left(\frac{p\pi}{W}\right)^2} \tag{1}$$

The numbers of half-cycle field variations along the x, y, and z directions are represented by m, n, and p, respectively.

2.1.2. Modal Analysis of Rectangular Antenna by Cavity Model Method

In this section, an initial rectangular patch antenna is designed on an FR4 substrate with relative permittivity and loss tangent values of $\epsilon_r = 4.3$, and $\tan\delta = 0.025$, respectively. We can theoretically calculate antenna design parameters (L, W) for orthogonal modes (TM^z_{010} & TM^z_{001}) and higher order modes by Equation (1) shown in Table 1, and the initial L, W parameters are calculated in the following manner.

(i) L-parameter calculation by TM^z_{010} ($m = 0, n = 1, p = 0$) at L5 (1176.45 MHz) using Equation (1);

$$(f_r)_{010} = \frac{1}{2\pi\sqrt{\mu\epsilon}}\sqrt{\left(\frac{0\pi}{h}\right)^2 + \left(\frac{1\pi}{L}\right)^2 + \left(\frac{0\pi}{W}\right)^2} = \frac{c}{2L\sqrt{\epsilon_r}}, \quad L = \frac{3*10^8}{2*1176.45*10^6\sqrt{4.3}} = 61.48\,\text{mm}.$$

(ii) W-parameter calculation by TM^z_{001} ($m = 0, n = 0, p = 1$) at L5 (1575.42 MHz) using Equation (1);

$$(f_r)_{001} = \frac{1}{2\pi\sqrt{\mu\epsilon}}\sqrt{\left(\frac{0\pi}{h}\right)^2 + \left(\frac{0\pi}{L}\right)^2 + \left(\frac{1\pi}{W}\right)^2} = \frac{c}{2W\sqrt{\epsilon_r}}, \quad W = \frac{3*10^8}{2*1575.42*10^6\sqrt{4.3}} = 45.91\text{mm}.$$

Table 1. Calculation of modes frequency for rectangular initia.

Modes (at $L = 61.48$ mm and $W = 45.91$ mm)	(m, n, p)	$(f_r)_{mnp} = \frac{1}{2\pi\sqrt{\mu\epsilon}}\sqrt{\left(\frac{m\pi}{h}\right)^2 + \left(\frac{n\pi}{L}\right)^2 + \left(\frac{p\pi}{W}\right)^2}$
TM^z_{010}	010	1176.45 MHz
TM^z_{001}	001	1575.42 MHz
TM^z_{011}	011	1921.46 MHz
TM^z_{020}	020	2352.95 MHz

2.2. Modal Analysis of Antenna Using Characteristic Mode Analysis

2.2.1. Brief Theory of Characteristic Modes Analysis

The characteristic modes analysis (CMA) theory introduces a complete set of orthogonal real currents modes for arbitrarily shaped conducting bodies. The CMA approach is independent of any type of excitation and is solely reliant on the shape and size of any conducting body. The characteristic modes are calculated numerically using the Method of Moments (MoM), which is based on surface integration equations. This methodology paves the way for a systematic antenna design compared to other automated optimization methods or trial-and errors, which do not provide any physical characteristics of antennas [26, 27]. The following two factors need to be considered when antenna modal analysis is performed:

(i) The MSn (Modal Significance for n mode) is determined using the equation below.

$$\text{MS} = \left|\frac{1}{1 + j\lambda_n}\right| \tag{2}$$

When MSn $> 1/\sqrt{2}$, the modes have a role in radiation. It is impacted by the shape and size of the conducting body in the absence of excitation and represents the normalised amplitude of current mode characteristics [28].

(ii) The CA (Characteristics Angle) is determined using the equation below.

$$\alpha = 180^\circ - \tan^{-1}(\lambda_n) \tag{3}$$

From the physical point of view CA represents the phase difference between characteristic current and associated characteristics field. When $\alpha_n = 180^\circ$ it represents that the nth mode is at resonance. For inductive mode the range of CA is $90^\circ < \alpha_n < 180^\circ$, and it stores magnetic energy. For capacitive mode, the range of CA is $180^\circ < \alpha_n < 270^\circ$, and it stores electric energy. The radiating bandwidth can be obtained from slope at 180° of characteristic angle curve [26]. λ_n are eigenvalues for the nth mode and given by following weighted eigenvalue equation as:

$$[X]\overrightarrow{J_n} = \lambda_n[R]\overrightarrow{J_n} \tag{4}$$

where J_n are the conducting body's characteristic modes currents, and R and X are the real and imaginary parts of the impedance matrix obtained by MoM. The eigenvalue represents the ratio of energy stored near the structure to radiated energy corresponding to the nth mode.

$$\lambda_n = \frac{\langle J_n^* X(J_n)\rangle}{\langle J_n^* R(J_n)\rangle} = \frac{P_{reac,n}}{P_{rad,n}} \tag{5}$$

where $*$ is the conjugate operator. The magnitudes of eigenvalues $\lambda_n(-\infty \text{ to } +\infty)$ provide radiating characteristics of any conducting structure at $\lambda_n = 0$, and all energy is radiated for the nth resonance mode. In the case for $\lambda_n > 0$, the energy is stored in the form of magnetic energy, and associated mode is inductive. For $\lambda_n < 0$, the stored energy in the form of electric energy and associated mode is capacitive [29]. For a given conducting body, the total electric surface current with excitation is a sum of linear combination of characteristic modes current J_n given as [30].

$$J = \sum_{n=1}^{N} \alpha_n J_n \tag{6}$$

where α_n is the modal weighting coefficient contributed by n_n mode obtained as:

$$\alpha_n = \frac{\langle J_n E^i\rangle}{\langle 1 + j\lambda_n\rangle} = \frac{V_n^i}{1 + j\lambda_n} \tag{7}$$

V_n^i is modal excitation coefficient and given as [31]:

$$V_n^i = \langle J_n E^i\rangle = \oiint J_n E^i ds \tag{8}$$

The input admittance Y_{in} of an antenna in the case of feed excitation is the ratio of current to voltage at feed location and given as [31]:

$$Y_{in} = \frac{I_{in}}{V_{in}} = \frac{\sum \alpha_n J_n^p}{E_{in}^p} = \sum \frac{(j_n^p)^2}{1 + j\lambda_n} = \sum Y_{in}^n \tag{9}$$

where J_n^p and E_{in}^p are current and electric field excited at feeding point of antenna. According Equation (9) Y_{in} is the sum of admittances of each mode, which is excited by feed with Z_o input impedance, and the corresponding reflection coefficient Γ_n is given as:

$$\Gamma_n = \frac{\left(\frac{1}{Y_{in}^n}\right) - Z_o}{\left(\frac{1}{Y_{in}^n}\right) + Z_o} \tag{10}$$

Equations (6) to (10) represent coupling behaviour between the nth characteristics modes and excitation (incident field of feed excitation).

2.2.2. Modal Analysis of Rectangular Antenna by CMA

The initial rectangular antenna performed modal analysis up to five modes uses the same parameters ($L = 61.48\,\text{mm}$ and $W = 45.91\,\text{mm}$) as those used in the Cavity Model Method. Figure 2(a) shows modal significance values of rectangular antenna, and corresponding mode-1, mode-2, mode-4, and mode-5 of rectangular antenna have MSn values close to one, which are responsible for radiation (due to MSn $> 1/\sqrt{2}$). However, mode-3 has MS value of near zero, so it is not responsible for radiation and stores magnetic energy (due to $\lambda_n > 0$) shown in Figure 2(b). Mode-1 and mode-2 have eigenvalues close to zero ($\lambda_n \approx 0$) from 1000 MHz to 3000 MHz, and the energies stored in mode-4 and mode-5 are in the form of electric energy (due to $\lambda_n < 0$) from 1000 MHz to 1910 MHz. After 1910 MHz, they are responsible for energy radiation (because eigenvalues are $\lambda_n \approx 0$) shown in Figure 2(b).

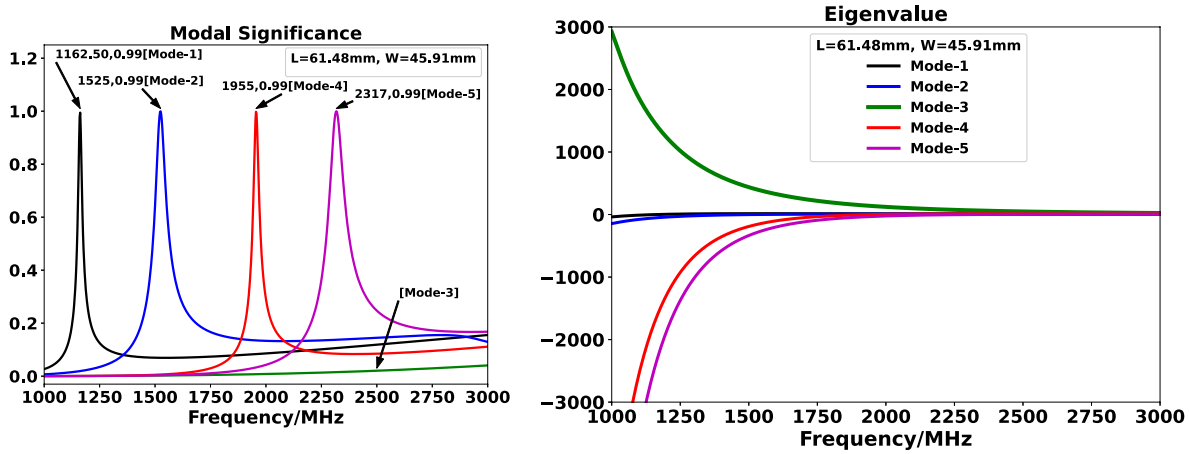

(a) (b)

Figure 2. Modal analysis plot of rectangular antenna by CMA. (a) Modal significance plot. (b) Eigen value plot.

Table 2 compares the theoretically cavity model approach with the practically CMA approach up to five modes with initial antenna dimensions ($L = 61.48\,\text{mm}$ and $W = 45.91\,\text{mm}$). The simulated resonance frequencies by CMA methods are much less deviated from those predicted by the theoretically cavity model method up to five modes. As a result, there is a good agreement between the theoretical cavity model method and practical CMA, with an average percentage error (APE) value around 1.86 percentage points.

Table 2. Comparative study between theoretically CMM and practically CMA technique.

Mode Frequency (MHz) by CMM	Mode Frequency (MHz) by CMA	PE $= \frac{\lvert f_{\text{CMM}} - f_{\text{CMA}} \rvert}{f_{\text{CMM}}}$
1176.45 (TM^z_{010})	1162.50 (Mode-1)	1.18
1575.42 (TM^z_{001})	1525 (Mode-2)	3.20
1921.46 (TM^z_{011})	1955 (Mode-4)	1.58
2352.95 (TM^z_{020})	2317.50 (Mode-5)	1.50
Average (APE)	=	1.86

Figure 3 shows the electric field patterns generated by the cavity model approach and the CMA, which are similar for equivalent modes. We can see that TM^z_{010} (mode-1) is the dominant mode, while TM^z_{001} (mode-2) is an orthogonal mode with hemispherical radiation patterns. So we can use TM^z_{010}

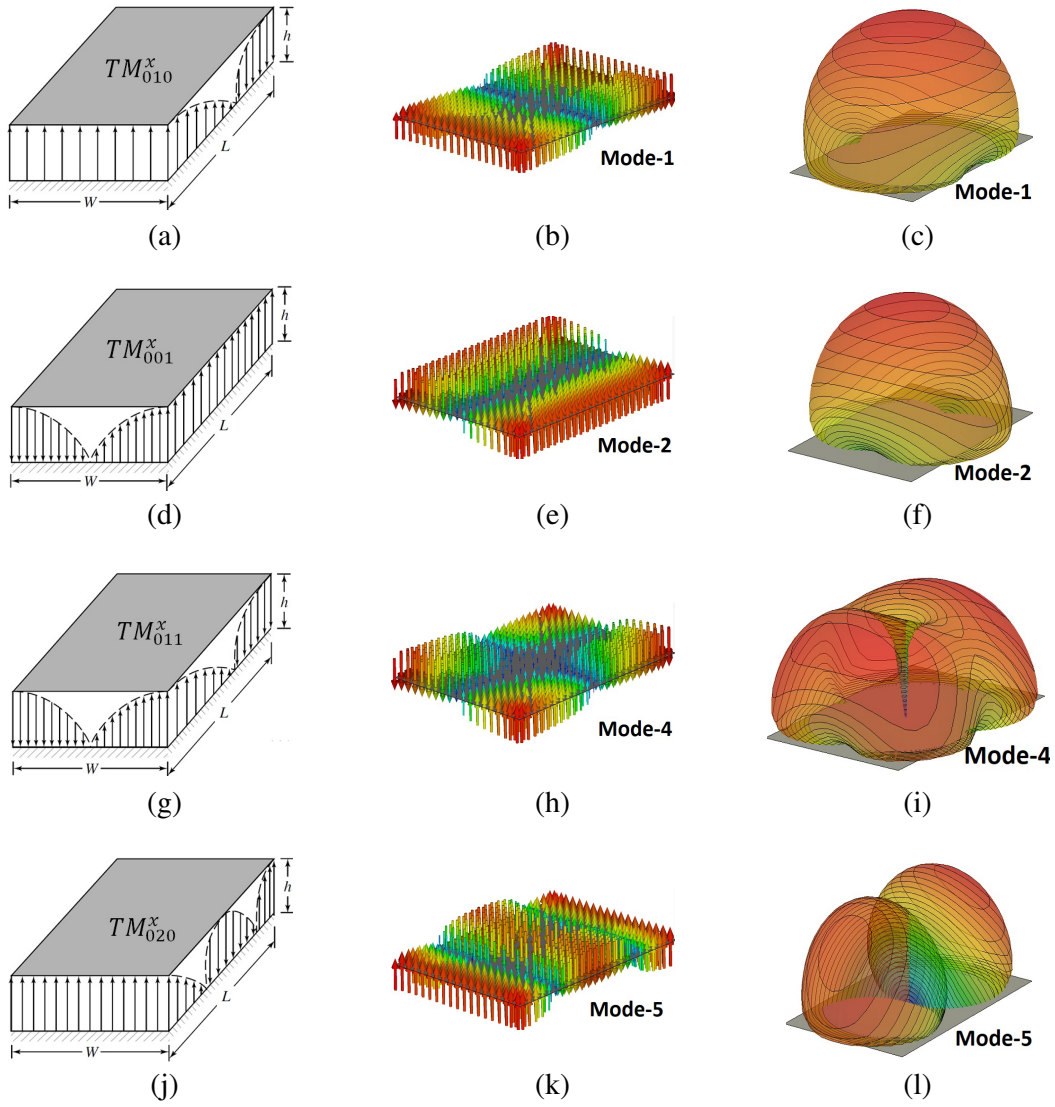

Figure 3. Comparative Study between theoretically CMM and practically CMA technique at $L = 64.19\,\text{mm}$, $W = 45.91\,\text{mm}$, (a) E-field by CMM at 1176.45 MHz, (b) E-field by CMA at 1162.50 MHz, (c) far field by CMA at 1162.50 MHz, (d) E-field by CMM at 1575.42 MHz, (e) E-field by CMA at 1525 MHz, (f) far field by CMA at 1525 MHz, (g) E-field by CMM at 1921.46 MHz, (h) E-field by CMA at 1955 MHz, (i) far field by CMA at 1955 MHz, (j) E-field by CMM at 2352.95 MHz, (k) E-field by CMA at 2317.50 MHz, (l) far field by CMA at 2317.50 MHz.

and TM^z_{001} modes for L5-band (IRNSS) and L1-band (GPS) application. The remaining higher order modes (mode-4 and mode-5) do not have hemispherical radiation characteristics, hence the rectangular antenna shape needs to be modified further to give tri-bands, L5-band, L1-band, and S-band, with hemispherical radiation characteristics.

3. DEVELOPMENT OF TSTB ANTENNA BY CMA METHOD

After understanding the field patterns and radiation patterns of the initial antenna using the cavity model method and CMA methods, this section discusses the design procedure of the proposed TSTB antenna using the CMA technique.

3.1. Parametric Study of Antenna-1

Figure 5(a) depicts the parametric analysis of Antenna-1 for $L = 58$, 60, and 62 mm with a constant $W = 43$ mm, as shown in Figure 4(a). In this plot, mode-1, mode-2, and mode-4 are significant for radiation (due to MSn $> 1/\sqrt{2}$) with different values of L, but mode-3 is not significant for radiation (due to MSn $< 1/\sqrt{2}$). Modes-1 and mode-4 are more vulnerable to changes in L, but mode-2 is more stable. Similarly, Figure 5(b) depicts a modal significance plot for a parametric study of Antenna-1 for $W = 41$, 43, and 45 mm with constant $L = 60$; in this case, modes-2 and mode-4 are more vulnerable to variations in W, whereas mode-1 is stable. After the parametric analysis of L and W from Figures 5(a) and (b), the optimal values of Antenna-1 are $L = 60$ mm and $W = 43$ mm, with resonance mode frequencies of 1176 MHz, 1575 MHz, and 2050 MHz, respectively.

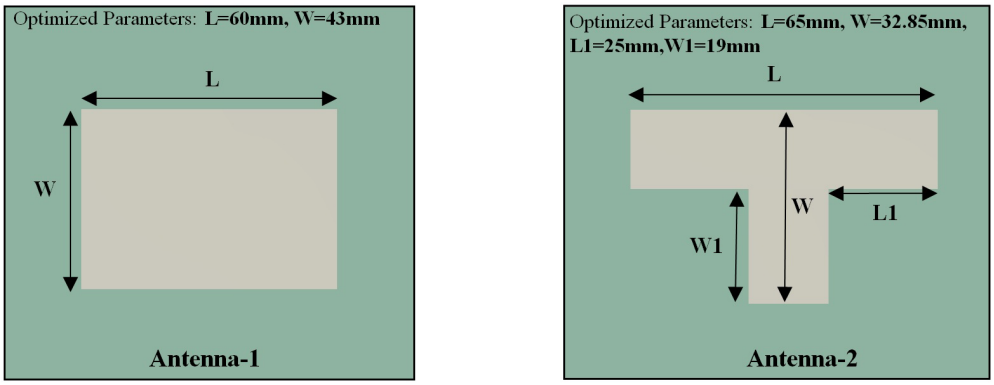

Figure 4. Schematic of Antenna-1 and Antenna-2 by CMA. (a) Antenna-1, (b) Antenna-2.

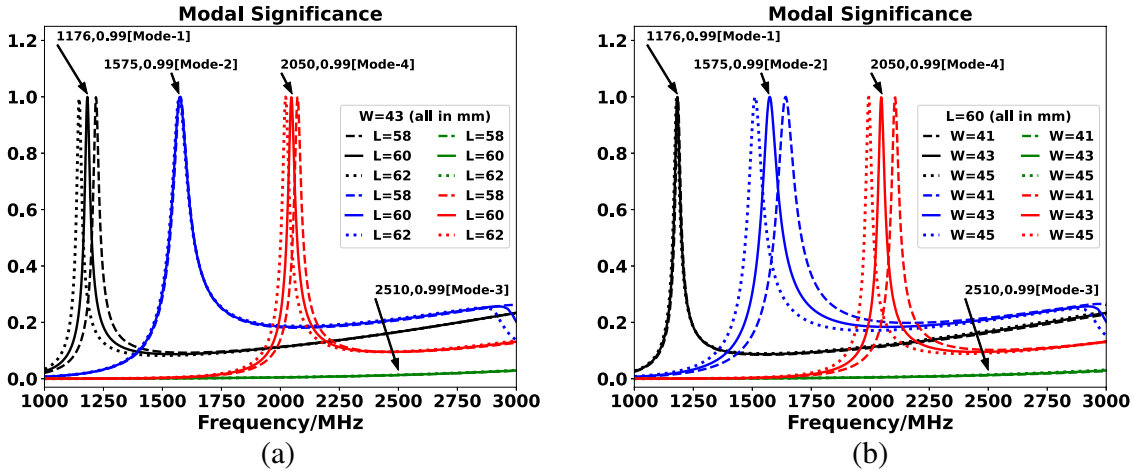

Figure 5. Modal significance plots of Antenna-1. (a) With different values of L ($W = 43$ mm), (b) with different values W ($L = 60$ mm).

Figure 6 depicts the surface current distribution and radiation patterns up to four modes. The radiation patterns of mode-1 and mode-2 are orthogonal with broadside radiation patterns due to surface current arrows being orthogonal (shown by black solid lines) and nulls (shown by red solid lines) being at the edges of the antenna, but mode-4 does not have broadside radiation due to the presence of out-of-phase surface current nulls (shown by red dash line) at the center of the antenna. Mode-3 is the magnetic mode and stores magnetic energy due to a closed loop of surface currents and nulls at

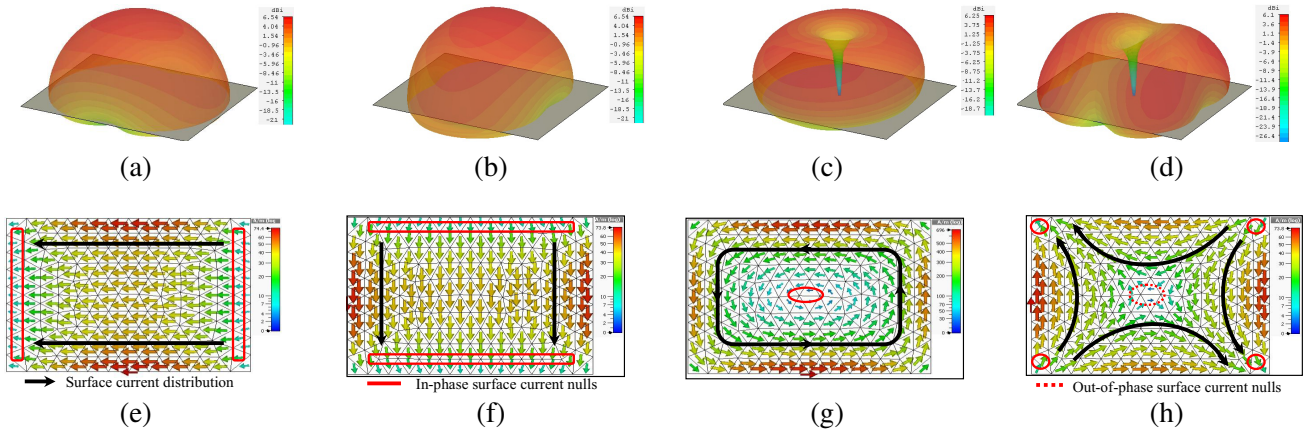

Figure 6. Modal surface current distribution and radiation patterns of Antenna-1, (a) far field at 1176 MHz (Mode-1), (b) far field at 1575 MHz (Mode-2), (c) far field at 2050 MHz (Mode-3), (d) far field at 2050 MHz (Mode-4), (e) surface current at 1176 MHz (Mode-1), (f) surface current at 1575 MHz (Mode-2), (g) surface current at 2050 MHz (Mode-3), (h) surface current at 2050 MHz (Mode-4).

the centre antenna, so this mode is not responsible for any radiation. Antenna-1 is desirable for the L5-band (1176 MHz) and L1-band (1575 MHz) from mode-1 and mode-2, but for the S-band we need further modification of Antenna-1.

3.2. Parametric Study of Antenna-2

It is not possible to shift mode-4 at S-band with broadside radiation pattern without modification in Antenna-1. So, we need arrange surface current on the antenna structure in such a way that Antenna-2 resonates at the desired tri-bands with enhanced higher-order mode radiation pattern. Antenna-1 is modified using the CMA technique to achieve tri-band characteristics as shown in Figure 4(b). The modal significance plot of the parametric analysis of Antenna-2 for $L1 = 23$, 25, and 27 mm with constant $W1 = 19$ mm is shown in Figure 7(a). For radiation, modes-1, mode-2, and mode-3 are significant (due to MSn $> 1/\sqrt{2}$) in this figure, but mode-4 is not significant for radiation (due to MSn $< 1/\sqrt{2}$), and variations in $L1$ affect mode-1, mode-2, and mode-3. Similarly, Figure 7(b) depicts the modal significant plot for the parametric study of Antenna-2 for $W = 17$, 19, and 21 mm with constant $L1 = 25$ mm;

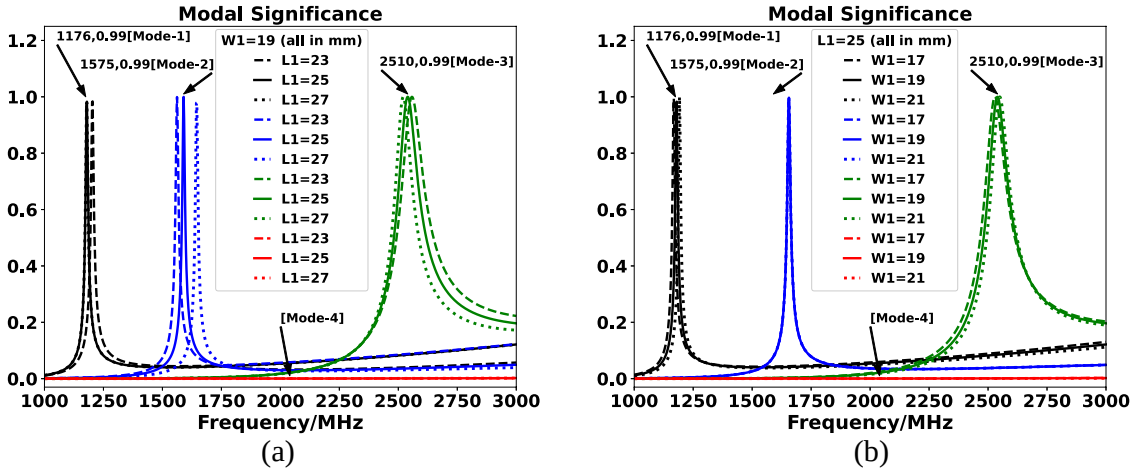

Figure 7. Modal significance plots of Antenna-2. (a) With different values of $L1$ ($W1 = 19$ mm), (b) with different values $W1$ ($L1 = 25$ mm).

mode-1 and mode-3 are vulnerable to variations in $W1$, while mode-2 is stable. The optimal values of $L1$ and $W1$ are 25 mm and 19 mm, respectively, based on the parametric analysis of $L1$ and $W1$ shown in Figures 7(a) and (b), with resonance mode frequencies of 1176 MHz, 1575 MHz, and 2510 MHz.

Figure 8 illustrates the surface current distribution and radiation patterns of Antenna-2 in up to four modes. The mode's significant parts of the surface current for each mode are represented by black solid line arrows. In this figure, the radiation patterns of mode-1 and mode-2 are orthogonal with broadside radiation patterns due to surface current arrows being orthogonal (shown by black solid lines). Mode-3 also has broadside radiation characteristics due to out-of-phase surface current nulls shifted near the antenna's corner instead of the center, as shown in Figure 8(g). The radiation patterns of the higher-order mode (mode-3) are converted from conical (shown in antenna-1) to broadside direction by reshaping the antenna structure with the help of surface current studies.

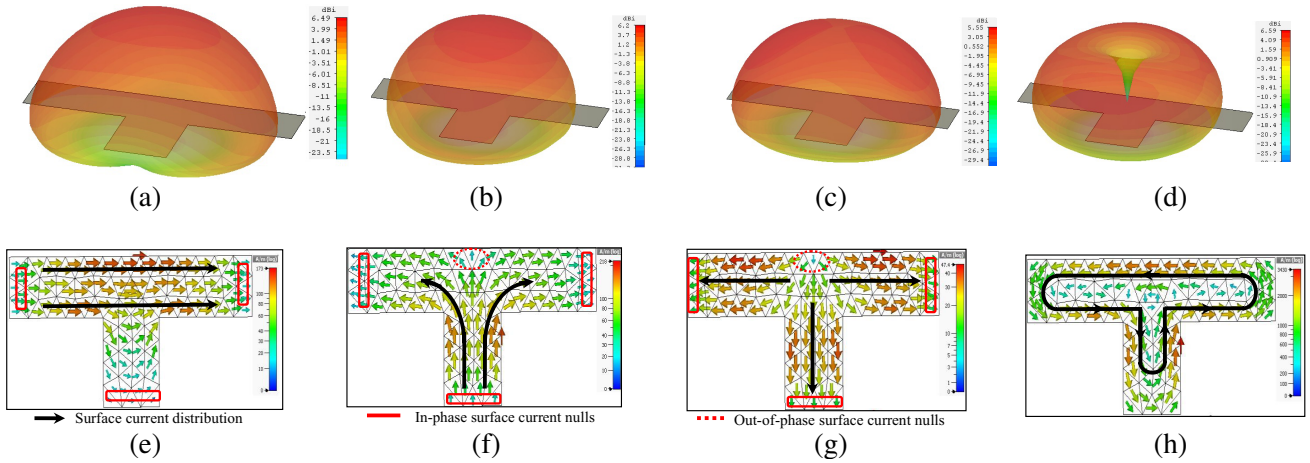

Figure 8. Modal surface current distribution and radiation patterns of Antenna-2, (a) far field at 1176 MHz (Mode-1), (b) far field at 1575 MHz (Mode-2), (c) far field at 2510 MHz (Mode-3), (d) far field at 2510 MHz (Mode-4), (e) surface current at 1176 MHz (Mode-1), (f) surface current at 1575 MHz (Mode-2), (g) surface current at 2510 MHz (Mode-3), (h) surface current at 2510 MHz (Mode-4).

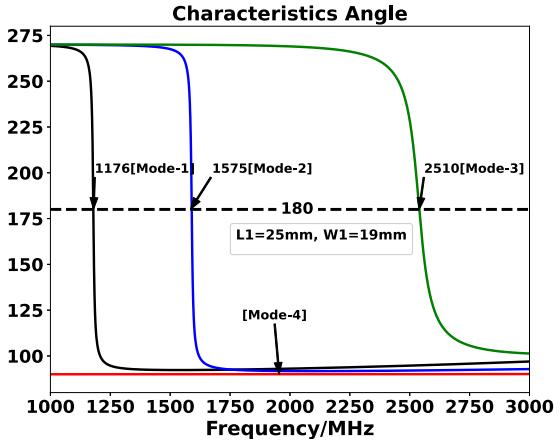

Figure 9. Characteristics angle plot of Antenna-2.

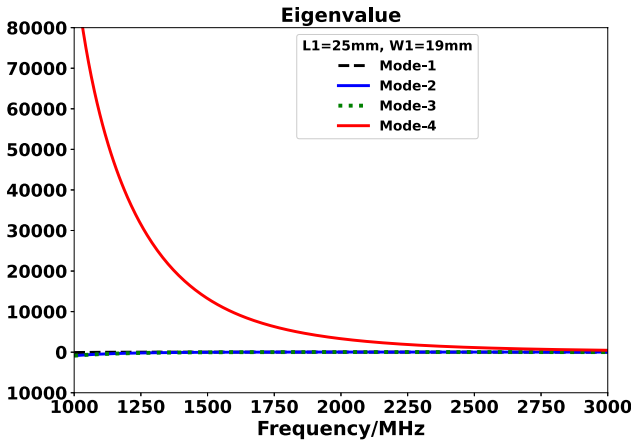

Figure 10. Eigen value plot of Antenna-2.

Figure 9 depicts the characteristic angle of optimized Antenna-2; in this plot, the characteristic angles of mode-1, mode-2, and mode-3 are close to 180° (CA $\approx$ 180°), which is a desirable condition for mode radiation. The eigenvalue plot of optimised Antenna-2 is shown in Figure 10, which shows that the eigenvalues of modes-1, mode-2, and mode-3 are near zero ($\lambda_n \approx 0$), while mode-4 has an

eigenvalue $\lambda_n > 0$, indicating that mode-4 stores magnetic energy. Finally, the tri-band characteristics are obtained by separating two orthogonal modes for the L5- and L1-bands, and one S-band is obtained through modification and surface current study of antenna-1 using CMA. In general case, higher order modes are not suitable for radiation due to low efficiency and instability in radiation pattern shown in Figures 3(i), (l). So in this work, radiation patterns are stable for all desired frequencies.

4. FULL-WAVE SIMULATION OF PROPOSED TSTB ANTENNA WITH EXCITATION

Figure 11 depicts the geometry of the optimised TSTB antenna with coaxial feed, and Table 3 lists the final design parameters. Figure 12(a) depicts an S_{11} plot parametric analysis of coaxial feed position for $X_o = -2.9$, -4.9, and -6.9 mm with constant $Y_o = 3.41$ mm, whereas Figure 12(b) depicts an S_{11} plot parametric analysis of coaxial feed position for $Y_o = 3.41$, 5.41, and 7.41 mm with constant $X_o = -6.9$ mm. So the best optimum coaxial feed location parameters values of $X_o = -6.9$ mm and $Y_o = 3.41$ mm are shown in Figures 12(a) and (b), and at this location mode-1, mode-2, and mode-3 are excited at 1174 MHz, 1575 MHz, and 2495 MHz. As shown in Figure 13, the excited modes with feed in antenna-1 are mode-1, mode-2, and mode-4 at 1170 MHz, 1580 MHz, and 2040 MHz, respectively.

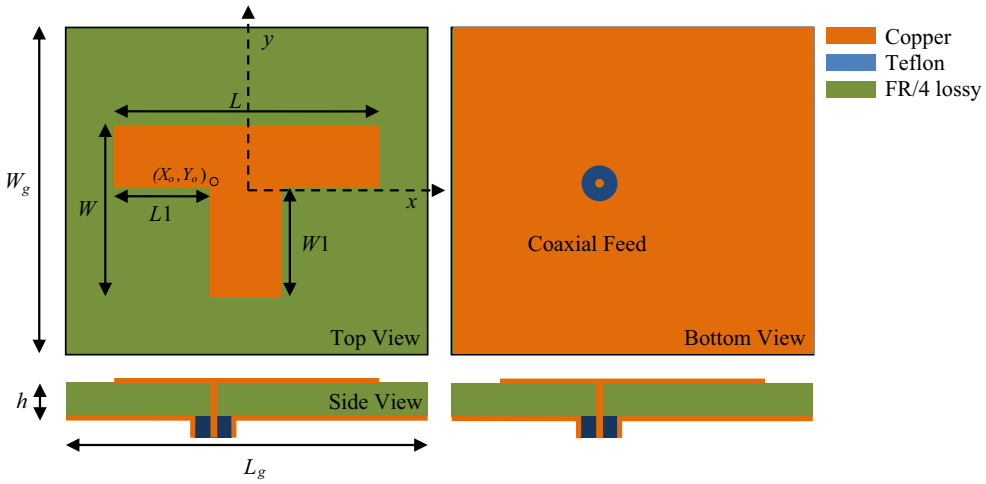

Figure 11. Proposed TSTB antenna with coaxial feed.

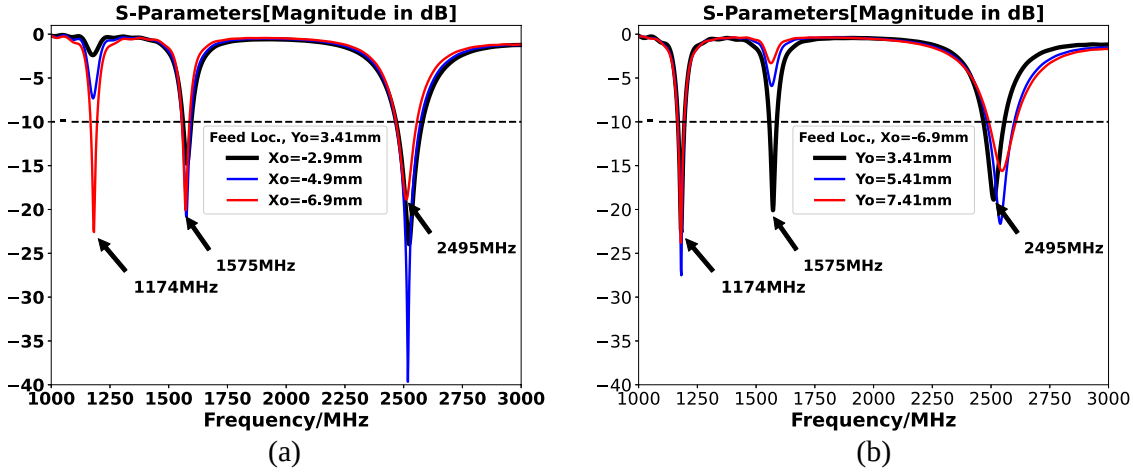

Figure 12. S_{11} of TSTB antenna with different values of X_o and Y_o. (a) With different values of X_o ($Y_o = 3.41$ mm), (b) with different values of Y_o ($X_o = -6.9$ mm).

Table 3. TSTB antenna design parameters.

Parameters	Value (mm)	Parameters	Value (mm)
W	32.85	W_g	100
L	65	L_g	100
$W1$	19	X_o	-6.9
$L1$	25	Y_o	3.41
h	3.20		

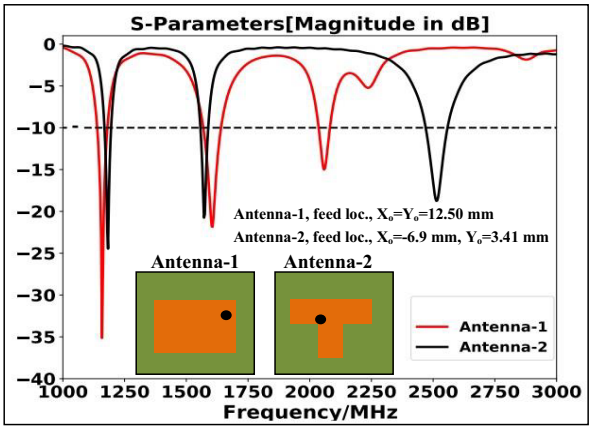

Figure 13. Scattering plot of Antenna-1 and Antenna-2.

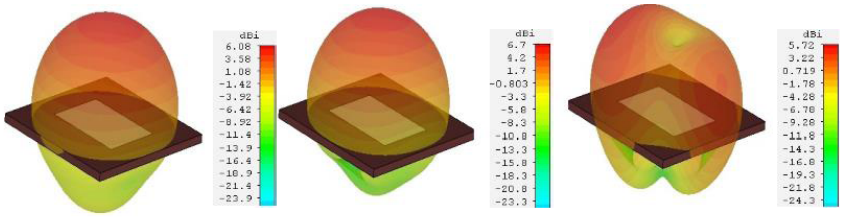

(f) 1170 MHz (e) 1580 MHz (d) 2040 MHz

Antenna-1

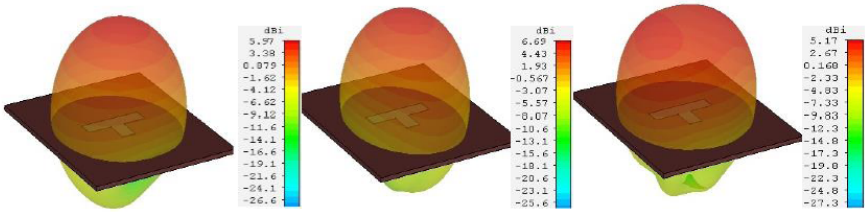

(a) 1174 MHz (b) 1575 MHz (c) 2095 MHz

Antenna-2

Figure 14. Simulated antennas peak gain.

The comparison of simulated far-field radiation patterns between Antenna-1 and Antenna-2 is shown in Figure 14. At 1174 MHz and 1575 MHz, Antenna-1 has a broadside radiation pattern, while at 2040 MHz, it has the lowest gain in the broadside direction. The radiation characteristics of Antenna-2 are hemispherical and stable for each band, with gains of 5.97 dBi, 6.69 dBi, and 5.17 dBi, respectively.

Table 4 shows the comparison of resonant frequencies between CMA without excitation and full-

Table 4. Comparative study between CMA without feed and full wave with feed.

Frequency (CMA (Without feed))	Frequency (Full wave (With feed))
1176 MHz	1174 MHz
1575 MHz	1575 MHz
2510 MHz	2495 MHz

wave simulation with coaxial feed excitation. There is a minimum deviation between CMA (MoM) and full-wave simulation (FIT) because MoM uses surface meshing without feed, and FIT uses hexahedral meshing with feed.

5. FABRICATION, MEASUREMENT, AND VALIDATION OF PROPOSED ANTENNA

The proposed TSTB antenna configuration was printed on FR4 material ($e_r = 4.3$, loss tangent = 0.025), and its volume is $100 * 100 * 3.2\,\text{mm}^3$, as illustrated in Figures 15(a), (b). The coaxial line is connected through an SMA connector, which is soldered at the bottom of the antenna. Figure 16 depicts simulated scattering parameters (S_{11}) between FIT (Finite Integration Technique) by CST EM-tool and FEM (Finite Element Method) by HFSS EM-tool, and these results are validated by measured result, with depicted VNA (Vector Network Analyzer) hardware setup in Figure 15(c). Figure 17 shows the simulated and measured peak gain plots. The TSTB antenna's observed resonance frequencies are 1174 MHz,

(a) (b) (c)

Figure 15. Photographs of fabricated antenna prototype, and its measurements set-up. (a) Top view, (b) bottom view, (c) VNA and anechoic chamber set-up.

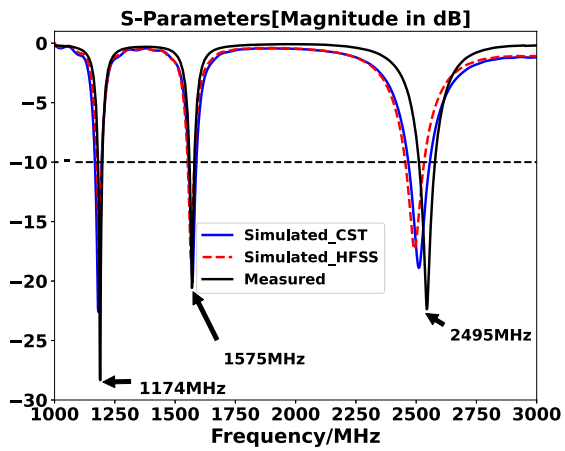

Figure 16. Scattering parameter (S_{11}) of TSTB antenna.

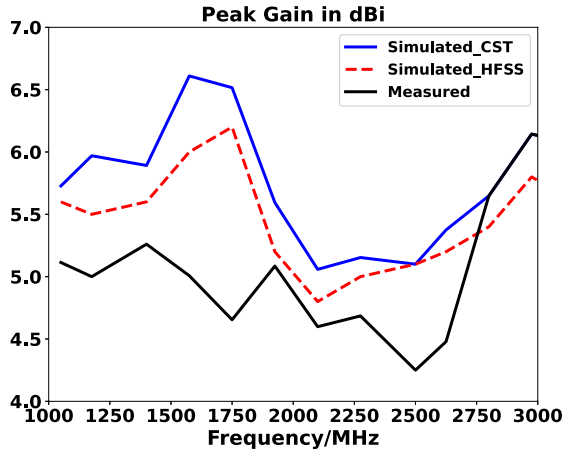

Figure 17. Simulated and measurement peak gain.

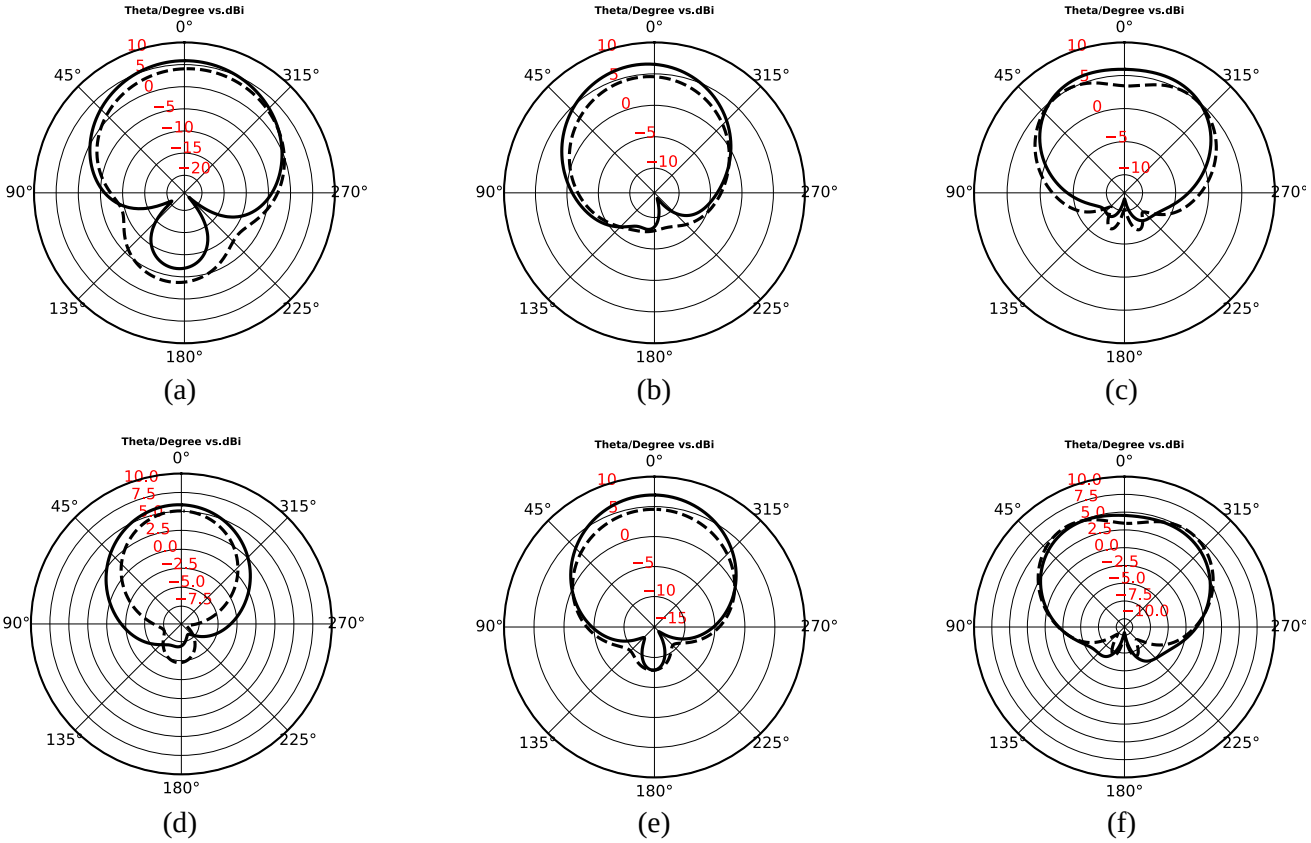

Figure 18. Simulated (solid line) and measurement (dashed line) radiation pattern of proposed TSTB antenna. (a) $\phi = 90°$, 1174 MHz, (b) $\phi = 90°$, 1575 MHz, (c) $\phi = 90°$, 2495 MHz, (d) $\phi = 0°$, 1174 MHz, (e) $\phi = 0°$, 1575 MHz, (f) $\phi = 0°$, 2495 MHz.

1575 MHz, and 2495 MHz, with corresponding measured bandwidths of 24 MHz (1164–1188 MHz), 24 MHz (1563–1587 MHz), and 51 MHz (2484–2535 MHz). The measurements' findings are quite close to those of the simulation, with only minor deviations generated by the measurement environment and manufacturing imperfections. Figure 18 depicts the far-field measured and simulated radiation patterns with xz-plane (phi = 0) and yz-plane (phi = 90) at 1174 MHz, 1575 MHz, and 2495 MHz, as well as the hardware setup with anechoic chamber shown in Figure 14(c). A good agreement is reached between the simulated and measured results of the proposed TSTB antenna.

6. COMPARISON WITH STATE-OF-THE-ART OF MULTI-BAND ANTENNAS

Table 5 summarises a compressive comparison of the most recent multi-band navigational antennas. It demonstrates that the antenna, as reported in [32], is a quad-band multi-layered stacked patch antenna made of RT/Duriod material. The antenna described in [33] is a quad-band cylindrical dielectric resonator antenna (cDRA) with a ceramic aperture feed. According to [34], a short annular ring antenna made of Rogger and FR4 materials achieves multi-band characteristics. An elliptical patch with a pair of concentric slot rings in the ground is reported in [35] for multi-band antenna characteristics. All of the reported antennas have a multi-layered structure, expensive materials, and are difficult to fabricate due to their complexity. The multi-band properties of the proposed antenna are obtained by using a T-shaped antenna with a coaxial feed to excite orthogonal and higher-order radiating modes for L1-band, L5-band, and S-band. The antenna has advanced features such as single layer, ease of integration with RF circuit, printing on low cost and light weight FR4 material, stable radiation pattern for the desired bands, 50 ohm impedance matched with coaxial feed line, and fabrication design simplicity.

Table 5. Resonant frequency comparisons with CMA, full-wave, and measured.

Ref.	Resonance Frequency (MHz)	Multi-band Methodology	Peak Gain (dBi)	Bandwidth (%)	Dimensions (mm^3)	Substrate
[32]	1176, 1227, 1575, and 2300	Stacked Patch Structure	2.23, 2.91, 3.40, and 2.70	1.10, 1.00, 4.10, and 1.50	$80 * 80 * 6.32$	Roger R04003
[33]	1227/1575, 2400, and 2500	cDRA aperture feed	5 for all	11.65, 7.64, 7.01, and 7.1	$120 * 120 * 29.6$	Ceramic and FR4
[34]	1227, 1575, and 2492	Shorted annular rings	5 for all	Not Reported	$80.4 * 80.4 * 24.5$	Roger R04003 and FR4
[35]	1176, 1227, and 1575	Elliptical patch with slots rings in ground	5.94, 4.19, and 4.39	Not Reported	$172.37 * 96.38 * 3.17$	RT Duroid 5880
This Work	1174, 1575, and 2495	T-shaped with orthogonal and higher-order modes	5.1, 5.31, and 4.35	2, 1.52, and 2	$100 * 100 * 3.2$	FR4

7. CONCLUSIONS

A single coaxial feed T-shaped Tri-band (TSTB) antenna with desirable antenna characteristics for L5-band, L1-band, and S-band is demonstrated. The tri-band characteristics are achieved by segregating orthogonal modes for L5-band and L1-band, and S-band is achieved by exciting higher-order mode in broadside radiation pattern, and stable radiation patterns for all desired bands are achieved by surface current studies of the antenna structure. The characteristic mode analysis theory and cavity modal method are used to support the modal analysis of antenna structure. The CST studio suite and HFSS are used for antenna design and simulation. The final prototype of the antenna is printed on low cost FR4 material, and simulation results are verified with measured results. The designed antenna operates at 1174 MHz, 1575 MHz, and 2495 MHz, respectively, with impedance bandwidths of 24 MHz, 25 MHz, and 51 MHz. The designed antenna can be utilised in L1-band, L5-band, and S-band satellite receiver applications.

ACKNOWLEDGMENT

This work was supported by RTU (ATU) TEQIP-III in Rajasthan, India, under project sanction No. TEQIP-III/RTU (ATU)/CRS/2019-20/35. The authors would like to express their gratitude to the Government Mahila Engineering College in Ajmer for providing fabrication and measurement facilities.

REFERENCES

1. Pourbagher, M., J. Nourinia, and C. Ghobadi, "Circularly polarized printed crossed-dipole antenna using branch-line feed network for GPS applications," *AEU-International Journal of Electronics and Communications*, Vol. 120, 153226, 2020.
2. Karthick, M. and K. R. Kashwan, "Design of IRNSS receiver antennae for smart city applications in India," *2015 Global Conference on Communication Technologies (GCCT)*, 277–280, 2015.
3. Singh, J., F. L. Lohar, and B. S. Sohi, "Design of circular polarized patch antenna for NaviC receiver applications," *IOP Conference Series: Materials Science and Engineering*, Vol. 1033, 012039, 2021.
4. Shaw, M. and Y. K. Choukiker, "Frequency reconfigurable microstrip patch antenna for IRNSS applications," *2020 International Conference on Inventive Computation Technologies (ICICT)*, 878–880, IEEE, 2020.

5. Praveen Chandran, C. R., M. Ramesh, and S. Raghavan, "Dual-band rhcp stacked microstrip antenna for IRNSS receiver," *International Journal of Pure and Applied Mathematics*, Vol. 118, 47–59, 2018.
6. Reddy, B. S., V. Senthil Kumar, V. V. Srinivasan, and Y. Mehta, "Dual band circularly polarized microstrip antenna for IRNSS reference receiver," *2015 IEEE MTT-S International Microwave and RF Conference (IMaRC)*, 279–282, 2015.
7. Lohar, F. L., C. Dhote, Y. Solunke, and N. K. Suyan, "Design of circularly polarized irnss receiver antenna using characteristic mode analysis," *2019 IEEE Indian Conference on Antennas and Propagation (InCAP)*, 1–5, IEEE, 2019.
8. Shukla, S. B., K. A. Vidya, T. Chacko, and K. K. Mukundan, "Single feed stacked circularly polarized patch antenna for dual band NavIC receiver of launch vehicles," *2019 IEEE Indian Conference on Antennas and Propagation (InCAP)*, 1–5, IEEE, 2019.
9. Yan, Y., Q. Nan, C. Liu, Y. Zhang, and J. Li, "3D-printed hemispherical helix GPS antenna with stable phase center," *2019 International Applied Computational Electromagnetics Society Symposium-China (ACES)*, Vol. 1, 1–2, IEEE, 2019.
10. Boccia, L., G. Amendola, and G. Di Massa, "Performance evaluation of shorted annular patch antennas for high-precision GPS systems," *IET Microwaves, Antennas & Propagation*, Vol. 1, 465–471, 2007.
11. Qian, J. F., F. C. Chen, K. R. Xiang, and Q. Chu, "Resonator-loaded multi-band microstrip slot antennas with bidirectional radiation patterns," *IEEE Transactions on Antennas and Propagation*, Vol. 67, 6661–6666, 2019.
12. Wa'il, A., R. M. Shaaban, and A. Tahir, "Design, simulation and measurement of triple band annular ring microstrip antenna based on shape of crescent moon," *AEU-International Journal of Electronics and Communications*, Vol. 117, 153133, 2020.
13. Fertas, K., S. Tebache, F. Ghanem, S. Tedjini, and R. Aksas, "Non-conventional multiband patch antenna design with filtering aspect based on genetic algorithm," *IETE Journal of Research*, Vol. 66, 815–822, 2020.
14. Singhwal, S. S., B. K. Kanaujia, A. Singh, J. Kishor, and L. Matekovits, "Dual-band circularly polarized MIMO DRA for sub-6 GHz applications," *International Journal of RF and Microwave Computer-Aided Engineering*, Vol. 30, e22350, 2020.
15. Pietrenko-Dabrowska, A., S. Koziel, and M. A. Hasan, "Expedited yield optimization of narrow- and multi-band antennas using performance-driven surrogates," *IEEE Access*, Vol. 8, 143104–143113, 2020.
16. Sah, B. K., G. Singla, and S. Sharma, "Design and development of enhanced bandwidth multi-frequency slotted antenna for 4G-LTE/WiMAX/WLAN and S/C/X-band applications," *International Journal of RF and Microwave Computer-Aided Engineering*, Vol. 30, e22214, 2020.
17. Sharma, I. B., F. L. Lohar, R. K. Maddila, A. Deshpande, and M. M. Sharma, "Tri-band microstrip patch antenna for C, X, and Ku band applications," *Optical and Wireless Technologies*, 567–574, Springer, Singapore, 2018.
18. Tiwari, D., J. A. Ansari, A. K. Saroj, and M. Kumar, "Analysis of a miniaturized hexagonal Sierpinski Gasket fractal microstrip antenna for modern wireless communications," *AEU-International Journal of Electronics and Communications*, Vol. 123, 153288, 2020.
19. Anand, R. and P. Chawla, "A novel dual-wideband inscribed hexagonal fractal slotted microstrip antenna for C- and X-band applications," *International Journal of RF and Microwave Computer-Aided Engineering*, Vol. 30, No. 9, e22277, 2020.
20. Ryu, Y. H., J. H. Park, J. H. Lee, and H. S. Tae, "Multiband antenna using +1, 1, and 0 resonant mode of DGS dual composite right/left handed transmission line," *Microwave and Optical Technology Letters*, Vol. 51, 2485–2488, 2009.
21. Chakraborty, M., S. Chakraborty, P. S. Reddy, and S. Samanta, "High performance DGS integrated compact antenna for 2.4/5.2/5.8 GHz WLAN band," *Radioengineering*, Vol. 26, 71–77, 2017.

22. Patel, R., A. Desai, and T. K. Upadhyaya, "An electrically small antenna using defected ground structure for RFID, GPS and IEEE 802.11 a/b/g/S applications," *Progress In Electromagnetics Research Letters*, Vol. 75, 75–81, 2018.
23. Chen, S. C., W. S. Cai, C. I. Hsu, and L. C. Chou, "Low-profile WLAN MIMO PIFA antenna system for laptops with large screen," *IETE Journal of Research*, 1–9, 2019.
24. Chen, Y. and C. F. Wang, *Characteristic Modes: Theory and Applications in Antenna Engineering*, John Wiley & Sons, 2015.
25. Balanis, C. A., *Antenna Theory: Analysis and Design*, John Wiley & Sons, 2015.
26. Tran, H. H., N. N. Trong, and A. M. Abbosh, "Simple design procedure of a broadband circularly polarized slot monopole antenna assisted by characteristic mode analysis," *IEEE Access*, Vol. 6, 78386–78393, 2018.
27. Jaiverdhan, M. M. Sharma, R. P. Yadav, and R. Dhara, "Characteristic mode analysis and design of broadband circularly polarized CPW-fed compact printed square slot antenna," *Progress In Electromagnetics Research M*, Vol. 94, 105–118, 2020.
28. Mohanty, A. and B. R. Behera, "Investigation of 2-port UWB MIMO diversity antenna design using characteristics mode analysis," *AEU-International Journal of Electronics and Communications*, Vol. 124, 153361, 2020.
29. Zhang, Q., R. Ma, W. Su, and Y. Gao, "Design of a multimode UWB antenna using characteristic mode analysis," *IEEE Transactions on Antennas and Propagation*, Vol. 66, 3712–3717, 2018.
30. Ciafardini, J. P., E. A. Daviu, M. C. Fabrés, N. M. M. Hicho, J. A. Bava, and M. F. Bataller, "Analysis of crossed dipole to obtain circular polarization applying characteristic modes techniques," *2016 IEEE Biennial Congress of Argentina (ARGENCON)*, 1–5, 2016.
31. Zhang, Q. and Y. Gao, "Compact low-profile UWB antenna with characteristic mode analysis for UHF TV white space devices," *IET Microwaves, Antennas & Propagation*, Vol. 11, 1629–1635, 2017.
32. Falade, O. P., M. U. Rehman, X. Yang, G. A. Safdar, C. G. Parini, and X. Chen, "Design of a compact multiband circularly polarized antenna for global navigation satellite systems and 5G/B5G applications," *International Journal of RF and Microwave Computer-Aided Engineering*, Vol. 30, e22182, 2020.
33. Sharma, A., G. Das, S. Gupta, and R. K. Gangwar, "Quad-band quad-sense circularly polarized dielectric resonator antenna for GPS/CNSS/WLAN/WiMAX applications," *IEEE Antennas and Wireless Propagation Letters*, Vol. 19, 403–407, 2020.
34. Li, L., Y. Huang, L. Zhou, and F. Wang, "Triple-band antenna with shorted annular ring for high-precision GNSS applications," *IEEE Antennas and Wireless Propagation Letters*, Vol. 15, 942–945, 2015.
35. Mishra, S., S. Das, S. S. Pattnaik, S. Kumar, and B. K. Kanaujia, "Low-profile circularly polarized planar antenna for GPS L1, L2, and L5 bands," *Microwave and Optical Technology Letters*, Vol. 62, 806–815, 2020.